# Millennial-timescale thermogenic $CO_2$ release preceding the PETM

Shijun Jiang[1,2,*], Ying Cui[3,*], Yasu Wang[1], Maura De Palma[3], B. David A. Naafs[4], Jingxin Jiang[5], Xiumian Hu[5], Huaichun Wu[6], Runjian Chu[6], Yangguang Gu[7], Jiuyuan Wang[8], Yizhou Huang[4], Miquela Ingalls[9], Timothy J. Bralower[9], Shiling Yang[10], James C. Zachos[11], Andy Ridgwell[12]

[1]State Key Laboratory of Marine Resource Utilization in South China Sea, Hainan University, Haikou 570228, China

[2]Southern Marine Science and Engineering Guangdong Laboratory (Zhuhai), Zhuhai 519082, China

[3]Department of Earth and Environmental Studies, Montclair State University, Montclair, NJ 07043, USA

[4]Organic Chemistry Unit, School of Chemistry and School of Earth Sciences, University of Bristol, Bristol, UK

[5]State Key Laboratory of Mineral Deposit Research, School of Earth Sciences and Engineering, Nanjing University, Nanjing 210023, China

[6]School of Ocean Sciences, China University of Geosciences (Beijing), Beijing 100083, China

[7]South China Sea Fisheries Research Institute, Chinese Academy of Fishery Sciences, Guangzhou, China

[8]Department of Earth and Planetary Sciences, Yale University, New Haven, CT 06511, USA

[9]Department of Geosciences, The Pennsylvania State University, University Park, PA 16801, USA

[10]Key Laboratory of Cenozoic Geology and Environment, Institute of Geology and Geophysics, Chinese Academy of Sciences, PO Box 9825, Beijing 100029, China

[11]Department of Earth and Planetary Sciences, University of California, Santa Cruz, CA 95064, USA

[12]Department of Earth and Planetary Sciences, University of California, Riverside, CA 92521, USA

*Correspondence should be addressed to: cuiy@montclair.edu (Y. Cui) and ssj0047@my.fsu.edu (S. Jiang).

**Abstract**

Geologic records support a short-lived carbon release, known as the pre-onset excursion (POE), occurred shortly before the Paleocene-Eocene Thermal Maximum (PETM; ~56 Ma). However, the source and pace of the POE carbon release and its relationship to the PETM remain unresolved. Here we show a high-temporal-resolution stratigraphic record spanning the POE and PETM from the eastern Tethys Ocean that documents the evolution of surface ocean carbon cycle, redox and

eutrophication, confirming the global nature of the POE. Biomarkers extracted from the sedimentary record indicate a smaller environmental perturbation during the POE than that during the PETM in the eastern Tethys Ocean. Earth system modeling constrained by observed $\delta^{13}C$ and pH data indicates that the POE was driven by a largely thermogenic $CO_2$ source, likely associated with sill intrusions prior to the main eruption phase of the North Atlantic Igneous Province and possibly biogeochemical feedbacks involving the release of biogenic methane.

## Introduction

A holistic understanding of the carbon-climate dynamics of past warming events has important implications for $CO_2$-induced anthropogenic climate change. The Paleocene-Eocene Thermal Maximum (PETM; ~56 Ma) represents the largest disruption of the global carbon cycle in the Cenozoic[1], which led to 5–6 °C global warming[2, 3], ocean acidification[4], ocean deoxygenation[5, 6, 7, 8], and intensified tropical cyclones[9, 10]. The prominent 3–6‰ negative carbon isotope excursion (CIE) registered in both terrestrial and marine sections is consistent with major emissions (~2,000 to >13,000 Pg C) of $^{13}C$-depleted carbon to the atmosphere and/or ocean and on a time-scale of a few to no more than *ca*. 20 kyr[11, 12]. Recent work suggests that the North Atlantic Igneous Province (NAIP) and associated $CO_2$ emissions may have triggered the PETM[13, 14, 15], followed by carbon sequestration through organic carbon burial[16] and silicate weathering[17]. The PETM was proceeded by a transient warming

63 accompanied by a smaller CIE[18]—known as the pre-onset excursion (POE) and which
64 is recorded in terrestrial records from the Wyoming Bighorn Basin[18] together with
65 only a few shallow marine sections (Atlantic coastal plain, southwest Pacific Ocean,
66 the North Sea and the Pyrenean foreland basins)[19, 20, 21, 22, 23]. The POE is a short-lived
67 warming event that occurred about 38 kyr to >100 kyr[24] prior to the PETM onset with
68 an estimated duration of no more than a few centuries[19] to millennia[24]. As an
69 environmental precursor to the PETM, the POE is absent in deep-sea sedimentary
70 records because its short duration may have limited its preservation to surface and
71 shallow water records[19]. Resolving a global POE signal could be further complicated
72 by bioturbation, sediment mixing, and chemical burndown of deep-sea carbonates[4, 25],
73 which could only be understood by studying shallow marine and terrestrial sections.
74 The POE warming may represent an early warning signal on the instability of carbon
75 reservoirs and set the stage for a climatic threshold crossing occurred during the
76 PETM. Previous studies suggest that the PETM is modulated by astronomical
77 forcing[26, 27, 28], and linked with the POE via repeated, catastrophic $CO_2$ release[24], such
78 as methane hydrate dissociation[19], either as a direct response of the warming or via
79 positive feedback mechanisms. Furthermore, the close timing between the initial stage
80 of the NAIP and the POE suggests that volcanism and magmatism may also serve as a
81 viable trigger[29]. However, the global extent of the POE, its relationship with the
82 PETM and exact mechanisms that triggered the POE—whether from methane hydrate
83 release, volcanic activity, or orbital drivers—remain debated.

Here we report ultra-high-resolution biogeochemical records from a recently discovered coastal shallow marine section in the eastern Tethys that span both the POE and the PETM (Fig. 1). The Kuzigongsu section (39°45'10" N, 75°17'29" E) is located in the western Xinjiang Uygur Autonomous Region of China, which was covered by the Turan Sea—an arm of the Tethys Ocean during the early Paleogene (Fig. S1). The eastern Tethys was a restricted shallow-water carbonate platform environment[30], and a critical site for the formation of warm and saline intermediate water and the burial of organic matter[31]. Abundant calcareous nannofossils[32] and well-preserved organic matter and oyster shells (Fig. S2) allow for an integrated sedimentological, biogeochemical, isotopic, organic geochemical, and global carbon cycle modeling approach to unravel the paleoenvironmental evolution of the eastern Tethys during the POE and PETM, thus filling a critical spatial data gap and advancing knowledge on forcing and recovery mechanisms of ancient hyperthermals.

## Results and Discussion

### Astronomically tuned high-resolution PETM and POE records from the understudied eastern Tethys

The presence of the PETM within the Kuzigongsu section has been confirmed by calcareous nannofossil biostratigraphy[32] (the NP9/NP10 boundary). It occurs at 19.9 m (on a depth scale of 0 to 48 meters in Fig. 2) and corresponds to a ~ 6–8‰ negative carbon isotope excursion (CIE)—among the largest CIEs observed in shallow marine

105 sites[1]. The CIE magnitude is ~ 6.3‰ in carbonate[32], ~ 6.0‰ in organic matter, and
106 somewhat amplified in long-chain *n*-alkanes (~ 7.8‰), which is likely a result of an
107 enhanced hydrological cycle[33] and elevated $pCO_2$[19, 34]. The primary $\delta^{13}C_{carb}$ signal
108 should be well preserved, on the basis of: 1) the strong covariation between $\delta^{13}C_{carb}$
109 and $\delta^{13}C_{org}$ ($r^2 = 0.75$, $p < 0.001$; Fig. S3); 2) that most $\delta^{13}C_{carb}$ and $\delta^{18}O_{carb}$ data plots
110 within the area of primary carbonates[35] (Fig. S3), and 3) the existence of only a weak
111 correlation ($r^2 = 0.18$, $p < 0.001$, Fig. S3) between $\delta^{13}C_{carb}$ and Mn/Sr (a strong
112 correlation is an indicator of diagenetic alteration[36]).
113 The POE is found at ~ 8.4 m below the PETM onset within lower nannofossil
114 Zone NP9a[32] and occurs in a 1.2-meter-thick interval (10.3 to 11.5 m) characterized
115 by a –1 to –2.5‰ CIE (Fig. 2). Specifically, we observed CIEs of –2.5‰ in carbonate
116 and –2.1‰ in organic matter, but in contrast to the PETM, only ~ –1‰ in long-chain
117 *n*-alkanes. The relatively smaller recorded magnitude in the *n*-alkane record is likely
118 due to the lack of data at 10.8 m depth where $\delta^{13}C_{carb}$ and $\delta^{13}C_{org}$ values reach their
119 minima (Fig. 2).
120 Power spectrum analysis of the detrended magnetic susceptibility (MS) data
121 series shows significant peaks in wavelength at 0.8, 1.2, 1.9, 3, 5, 6.5, and 9.8 m (see
122 Methods, SI and Figs. S4–S6), with the filtered 1.2–1.9 m cycles interpreted as
123 precession signal with an assumed 21 kyr duration and the filtered 5 to 9.8 m cycles
124 as short eccentricity (~ 100 kyr). Spectral analysis revealed sedimentation rates
125 averaging between 6.0 and 8.3 cm $kyr^{-1}$ (Fig. S5) and suggests that the durations of

126 the PETM and the POE at our study site are ~ 127 kyr and ~ 21 kyr, respectively (age
127 model option 1; see SI and Table S2 for details). The PETM and POE are separated
128 by ~ 144 kyr (± 21 kyr). The estimated PETM duration of 127 kyr is shorter than
129 inferred from the deep sea sites (e.g., ~ 170 kyr from Röhl et al.[37] and Zeebe and
130 Lourens[38]), likely due to incomplete preservation of the entire PETM at Kuzigongsu
131 with a change in lithology that truncates the recovery phase. The POE onset duration
132 of ~7.0 kyr (age model option 1) is similar to, but slightly longer than the 2 to 5.5 kyr
133 estimated by Bowen et al.[18] (Fig. 4). An alternative age model option 2 that accounts
134 for the significant drop in wt.% $CaCO_3$ and a likely truncation assumes the filtered 6–
135 10 m cycles represent ~20 kyr precessional signal. This age model option provides a
136 duration of ~39 kyr for the PETM, ~4 kyr for the POE and ~54 kyr between the
137 PETM and POE, which suggests the study site only preserves the PETM onset and the
138 plateau, rather than the recovery (see SI for detailed discussion). However, due to the
139 uncertainty in the astronomically tuned age model, we assume that the POE onset
140 duration ranges from 500 to 7,000 years to cover the full range of reported values in
141 the literature[19, 24].
142
143 **Paleoenvironment of the eastern Tethys during the POE and PETM**
144 We use a multi-proxy approach to reconstruct the paleoenvironmental evolution of the
145 eastern Tethys during the POE and PETM. Our records (Figs. 2, 3) include C/N ratios
146 as indicators of organic matter source, weight percent (wt.%) $CaCO_3$ as a proxy for

147 ocean acidification and detrital dilution, trace element geochemistry for marine
148 nutrient and chemical weathering proxies, organic biomarkers as proxies for marine
149 microbial communities, and mercury content as a possible indicator of NAIP activity.
150 Together, our new data suggest that the shallow eastern Tethys experienced profound
151 environmental changes, including extreme warmth, eutrophication, and biological
152 turnover. Furthermore, the moderately high sedimentation rates (optimal
153 sedimentation rate fluctuates between ~ 6–8 cm $kyr^{-1}$; Figs. S4, S5) at this shallow
154 site (estimated water depth is ~ 30–50 m based on microfacies analysis and
155 foraminifera indicators[30]) yield highly expanded records that provide unique details
156 on the relationship between the PETM and the POE. Such details are generally
157 obscured in deep-sea sites because of lower sedimentation rates, dissolution, and
158 bioturbation[4, 39].

159 The section is characterized by a rapid decrease in wt.% $CaCO_3$ from >80
160 wt.% to near 0 wt.% at ~9 m—a shift which precedes the POE and PETM and may be
161 attributed to significant reduction of carbonate production, detrital dilution, or shallow
162 ocean acidification[4, 40]. The sharp decrease in oxygen isotopes of marine carbonate
163 values ($\delta^{18}O_{carb}$) (the magnitude of $\delta^{18}O_{carb}$ excursion is 2.5‰, from –3.6‰ to –6.1‰,
164 which corresponds to a temperature rise of 12.8 °C, much larger than the estimated
165 global temperature change of ~ 5.4–5.9 °C, ref. 3), while consistent with an abrupt
166 and significant warming during the POE and PETM (Fig. 2b), could be due to
167 diagenetic overprinting. Alternatively, the $\delta^{18}O_{carb}$ decrease may represent a decline in

168 local salinity as the $\delta^{18}O_{sw}$ at epeiric sites can be strongly influenced by freshwater
169 input from surrounding continents[2]. Clumped isotope data from a well-preserved
170 oyster specimen (at 29.8 m; Fig. S2) indicate that the eastern Tethys surface water
171 temperature was around 32.5 ± 1.5 ºC (1σ) at the recovery phase of the PETM (Fig.
172 2). This estimate is similar to our independent temperature estimate of 30.6 ± 4.5 ºC
173 (1σ) based on the $TEX_{86}^{H}$ proxy[41] for the sample at the same depth. However, the
174 thermal maturity is relatively high for this section and the cyclized isoGDGTs
175 abundance is low, preventing us from obtaining a high-resolution and precise $TEX_{86}^{H}$
176 temperature record at the site (Fig. 2).
177 In the organic matter fraction, peak TOC and C/N ratios coincide with the
178 lowest $\delta^{13}C_{org}$ values during the PETM, suggesting increased terrestrial organic matter
179 input at the study site, a likely consequence of intensified continental weathering
180 and/or higher terrestrial primary production[42]. The inferred increase in terrestrial
181 weathering is supported by the higher values of Ti/Al and K/Al ratios[43]. Elevated $C_{29}$
182 hopane ββ/(αβ+βα+αβ) ratios (average = 0.3) during the PETM indicate increased
183 input of fresh organic matter either due to higher primary productivity or increased
184 flux of fresh terrestrial organic matter into the basin (Fig. 3e). Lower $C_{29}$ hopane
185 ββ/(αβ+βα+αβ) ratios (average = 0.1) in the pre- and post-PETM samples suggest
186 relatively low primary production in the surface waters with background input of
187 reworked and more mature organic matter from the surrounding continents[42].
188 Similarly, Crenarchaeol/(Crenarchaeol+isoGDGT-0) ratios range from 0.1 to 1.0,

189 with a significant decrease during the POE and PETM. Crenarchaeol (with four
190 cyclopentane rings and one cyclohexane ring) is considered as a biomarker for
191 Thaumarchaeota[44]. The lower Cren/(Cren+isoGDGT-0) ratios during the POE and
192 PETM therefore likely reflect a reduction in marine Thaumarchaeota, which may be
193 attributed to warmer surface ocean temperature and lower dissolved oxygen
194 concentration[45]. The occurrence of 2-methylhopanes (2-MeHop) in the PETM interval
195 indicates a transient perturbation of surface ocean characteristics (Fig. 3). The $C_{29}$ 2-
196 MeHop Index, calculated as 100 × ($C_{29}$ 2-MeHop)/($C_{29}$ 2-MeHop + $C_{29}$ Hop)[46],
197 ranges from ~ 0–38% with two prominent peaks, at 20.9 m and 28.5 m respectively,
198 corresponding to the peak values of TOC and C/N ratios. Several studies reported that
199 the occurrence of 2-MeHop in the sedimentary record can be viewed as indicators of
200 stress responses to the capacity of microbial respiration under hypoxia[47], nitrogen
201 fixation[48], increased productivity[49], and changes in pH[50], corroborating the
202 interpretations of elevated primary productivity discussed above. Furthermore, the
203 anomalously high $C_{29}$ 2-MeHop Index during the PETM may be attributed to marine
204 nitrogen cycle perturbation as a result of biogeochemical changes. This is similar to
205 observations of other major carbon cycle perturbations of the Phanerozoic, such as the
206 end-Permian mass extinction event[51], the end-Triassic extinction event[52], and the
207 Mesozoic Oceanic Anoxic Events[53, 54].
208 Ocean deoxygenation may have been strengthened by increased primary
209 productivity from elevated nutrient input due to enhanced terrestrial weathering. This

suggestion is supported by negative Mn* values (Eq. 1) from the POE to the PETM (Fig. 3), which are associated with more reducing conditions due to significant redox-related changes in the solubility of Fe and Mn[55].

$$Mn^* = \log[(Mn_{sample}/Mn_{shales})/(Fe_{sample}/Fe_{shales})] \quad (1)$$

The values used for the $Mn_{shales}$ and $Fe_{shales}$ are 600 and 46,150 ppm, respectively[56]. Furthermore, the inferred surface ocean deoxygenation is consistent with elevated V/Al ratios over the same interval (Fig. 3) because V ions (+4 and +5 valence) are closely coupled with the redox cycle of Mn[57]. Widespread deoxygenation is well documented in many ocean basins across the globe during the PETM[5, 58], including the North Sea[59], the Arctic Ocean[60], the Atlantic and Caribbean[61, 62], and the northwestern Tethyan margins[63]. However, no significant changes in these redox indicators were observed across the POE[64], suggesting relatively stable redox conditions in the eastern Tethys at this time.

Mercury content (or Hg concentration normalized as a ratio to organic carbon content—Hg/TOC) has been used as a signal of NAIP activity by several previous studies[15, 65]. Our site exhibits two prominent Hg/TOC peaks that show a small lead in time relative to the onset of the POE (~ 11 kyr) and the PETM (~ 26 kyr) (Fig. 2), supporting a pulsed Hg input and a possible link between Hg source and the $^{13}C$-depleted carbon source. However, because of the overall low Hg concentrations at the study site, establishing a direct link between the NAIP and the Hg peaks is not straightforward. Low Hg is likely due to dilution by carbonate and detrital input, the

long distance of the site relative to Hg source, and/or Hg transport via oceanic waters rather than global atmospheric transport[15]. Increased Hg concentrations across the POE and PETM compared to background values suggest that multiple possible sources and processes may have been at play in addition to the NAIP activity. For example, variations in Hg concentrations in the sedimentary records can be caused by changes in river runoff, weathering, transport of terrestrial materials, primary productivity, source of organic matter, and post-depositional processes (*e.g.*, diagenesis and dissolution)[15], which could become more important at the study site because of its restricted carbonate platform setting[66]. Deoxygenation and changes in organic matter preservation and transport cannot fully account for the excess Hg as shown by the steeper Hg gradient to TOC within the PETM and POE interval at our site (Fig. S7). Moreover, Hg fluxes associated with wildfire (e.g., Arctic region[67], northeastern US margin[68], and England[69]) may have been far less than the Hg fluxes associated with a large igneous province event[70], and therefore cannot provide sufficient Hg into the study site. Principal component analysis (PCA) suggests that Hg is most closely related to C/N ratios (higher C/N ratio indicates more terrestrial organic source) and $\delta^{13}C_{org}$ during the PETM, which reflect changes in source of organic matter and $^{13}C$-depleted $CO_2$ emissions (Fig. S7). The C/N ratio exhibits no significant change across the POE, suggesting the increase in Hg and Hg/TOC ratio is unrelated to changes in source of organic matter. On the other hand, C/N ratio shows a large increase across the PETM, which indicates that changes in source of organic

252 matter may have contributed to the increased Hg concentrations. These potential
253 processes do not preclude volcanic involvement, however, especially via more
254 complex pathways than simple atmospheric loading and deposition[71]. Despite these
255 potential complex sources of Hg, we cannot completely exclude direct and indirect
256 involvement of the NAIP in driving the Hg changes in the study section[72]. For
257 example, the NAIP was active as early as 62 Ma[72], and its peak activity may have
258 encompassed both the POE and the PETM[73, 74, 75, 76]. A negative shift in $^{187}Os/^{188}Os$
259 ratios has been observed prior to the PETM in several sites globally[29, 72, 77, 78], lending
260 support to the occurrence of LIP activity prior to the PETM. Furthermore,
261 hydrothermal vent complexes in the northeast Atlantic region[79, 80] further support that
262 the NAIP activity can at least partially explain the observed Hg records.
263
264 **Thermogenic $CO_2$ emissions associated with NAIP activity during the POE**
265 The PETM carbon emission history has been extensively modeled in the past, with
266 estimated carbon emission rates ranging from 0.3 to 1.7 Pg C $yr^{-1}$ for a CIE onset
267 duration from 3,000 to 20,000 years and cumulative amount of carbon added ranging
268 from 2,500 to 13,000 Pg C[11, 12, 18, 80, 81, 82]. Because the carbon emission history
269 preceding the PETM has not been systematically quantified in an Earth system model
270 and very little is yet known about the $CO_2$ source during this time[19], we then focused
271 our model analysis on the POE (Table S3 and Fig. 4). Our new high-resolution

geochemical data, together with an orbitally tuned astronomical age model, provide a unique opportunity to assess the effects of $CO_2$ emissions during the POE.

We quantify carbon emissions over the POE using a data assimilation approach that considers paired $\delta^{13}C_{DIC}$-pH variation across the POE within an Earth system model of intermediate complexity cGENIE, following the approach detailed in Gutjahr et al.[12]. In this, changes with time in annual global mean surface ocean pH (derived from $\delta^{11}B$ proxy data from the Mid-Atlantic Coastal Plain with a change of ~ −0.1 to −0.3 pH units[19]) constrain the emission rate of $CO_2$ to the atmosphere. Similarly, the change with time in observed $\delta^{13}C$ of annual global mean surface ocean DIC ($\delta^{13}C_{DIC}$) (reconstructed by applying an anomaly derived from the $\delta^{13}C$ data of a global compilation; Fig. S8) refines the $\delta^{13}C$ value of the (pH-constrained) $CO_2$ emissions. The novelty of this approach is that it offers a unique solution of the mean $\delta^{13}C_{source}$ without having to make a specific assumption about the carbon source (e.g., compare with Cui et al.[11]; see Methods and SI for detailed model results and sensitivity tests). To account for the uncertainty in the POE onset duration, we place our records on four different age models, including age model option 1 and 2 from this study, an age model from the Bighorn Basin based on Bowen et al.[18] and an assumed age of 500 years based on Babila et al.[19] (a summary of our model results and sensitivity analyses for the POE is listed in Table S3). (Fig. 4).

The flux-weighted $\delta^{13}C_{source}$ values across the entire emission duration vary between −30.8 and −44.5‰ for the four age models used in our simulations with the

293 minimum change in pH suggested by Babila et al.[19], consistent with a thermogenic
294 $CO_2$ source[83] (–30 to –65‰; Fig. 4a-d and Table S5a). Longer POE duration (e.g.,
295 Age 1 associated with ~7,000 year POE onset) necessitates lower flux-weighted
296 $\delta^{13}C_{source}$ values (–44.5‰) over the entire emission interval (Fig. 4a) at slower
297 emission rate (~ 0.2 Pg C $yr^{-1}$). We note that the $\delta^{13}C_{source}$ values become
298 progressively lower from the POE onset, likely resulting from a faster rate of change
299 toward its minimum values in the $\delta^{13}C$ forcing. This may represent a shift from
300 thermogenic methane to biogenic methane (~ –34 to < –70‰[84, 85]) emissions during
301 the development of the POE. The average carbon emission rate over the entire
302 emission period ranges from 0.2 to 1.3 Pg C $yr^{-1}$ (Fig. 4e-h), comparable to those
303 estimated for the PETM from sill-degassed $CO_2$ and thermogenic methane (0.2 to 0.5
304 Pg C $yr^{-1}$ from Jones et al.[13]; 0.6 Pg C $yr^{-1}$ from Frieling et al.[80]). Larger magnitude of
305 pH changes (e.g., $\Delta pH$ = ~0.2 to 0.3) yield overall larger average peak $CO_2$ emission
306 flux (2.9 Pg C $yr^{-1}$) and higher average $\delta^{13}C_{source}$ values (–19.5‰) (Table S3), still
307 consistent with largely thermogenic methane source. The pH change for the POE has
308 only been documented at a single location utilizing a novel approach to measuring
309 boron isotopes ($\delta^{11}B$) and thus has a high uncertainty[19]. Considering the smaller
310 magnitude of $\delta^{13}C$ excursion, smaller degree of warming, its shorter duration, and
311 minor ecological responses, the changes in pH during the POE is unlikely to exceed
312 that during the PETM ($\Delta pH$ = ~0.3)[86]. Higher average carbon emission rate is

313 associated with shorter POE onset duration (Fig. 4e), which represents a combined
314 feature of the imposed ΔpH forcing and age models used (Fig. S8).

315 The cumulative $CO_2$ emission during the POE ranges from ~1,030 to 1,765 Pg
316 C (Fig. 4i-l), with peak $pCO_2$ reaching ~1,180 to ~1,220 ppm—a rise of ~350 to ~390
317 ppm above ~830 ppm (Fig. S9). The modeled cumulative carbon emitted during the
318 POE falls within the range of the 400 to 1,600 Pg C suggested by Babila et al.[19] using
319 similar ΔpH. However, if the actual ΔpH was at the lower end (lower than ~0.1), it is
320 more likely that the carbon source was primarily biogenic methane. Associated with
321 the diagnosed carbon emissions is a modelled global sea surface temperature rise (ΔT)
322 of ~1.1 to ~1.3 ºC (Fig. S9). Although the paleotemperature history of the POE is
323 currently poorly known, existing Mg/Ca ratios of planktonic foraminifera from the
324 mid-Atlantic coastal plain suggest that the surface ocean temperature increase was ~2
325 ºC with an uncertainty of ± 1 ºC due to salinity variations[19], consistent with our
326 modeled temperature changes within uncertainty. The POE warming may also help
327 explain the observed increase in warm-water coccolithophore taxa in the eastern
328 Tethys[32].

329 Thermogenic $CO_2$ related to the NAIP activities may have been the dominant
330 carbon sources during the POE via contact metamorphism by intrusive activity
331 through hydrothermal vent complexes[79]. It should be noted that mantle convection
332 models suggest that a peak NAIP carbon emission flux at ~0.5 Pg C $yr^{-1}$ could occur
333 between 1 and 20 kyr[13], comparable to those simulated in our inversion experiments,

334 despite the geochronology of the NAIP continental flood basalt sequences being not
335 very well constrained[72]. It is also important to note that a caveat of cGENIE in
336 interpreting our results is the lack of terrestrial biosphere and potential changes in
337 orbital forcing, which could impact the climate responses and lead to uncertainties in
338 carbon emission estimates. Although this study provides a range of estimates on the
339 carbon source and emission flux during the POE, more precise $\delta^{11}B$-based global
340 surface pH records, detailed history of the sill intrusion of the NAIP, sea surface
341 temperature records from across different latitudes, and better-constrained
342 geochronology of the NAIP activity are clearly needed to reduce the uncertainty of
343 the estimated thermogenic carbon emission fluxes from the NAIP.

344 The evolution of mean core-top carbonate ($CaCO_3$) with time in the model
345 exhibits a smaller magnitude of $\delta^{13}C$ decrease for simulations with bioturbation turned
346 on compared to those without bioturbation (Fig. S10). Similarly, core-top $CaCO_3$
347 wt.% also exhibits smaller degree of dissolution for experiments with bioturbation on
348 (Fig. S10). Longer experiment duration allows for a larger CIE magnitude regardless
349 of whether bioturbation is on. This is due to the combined effects of bioturbation and
350 dissolution as a result of the cumulative carbon emission (Fig. S10 and Fig. 4i-l),
351 supported by a comparable Eocene hyperthermal event[87]. These experiments support
352 the inference that short POE onset duration (less than millennial timescale) and
353 bioturbation are the main causes of the lack of POE signal in the deep-sea
354 sedimentary records.

In conclusion, we report astronomically tuned, ultrahigh-resolution PETM and POE stratigraphic records from a recently discovered site in the eastern Tethys. Geochemical proxies based on carbonate, bulk organic matter, and biomarkers suggest that the eastern Tethys experienced profound carbon cycle perturbations during the POE and PETM. Our integrated stratigraphic data and Earth system modeling together suggest that the millennial time-scale POE may be attributed to mainly thermogenic $CO_2$ emission associated with sill intrusion prior to the main eruption phase of the NAIP, with contributions from amplifying feedbacks such as biogenic methane release. The POE may have set the stage for the ecosystem threshold crossing and the extreme carbon cycle disruption occurred during the PETM.

## Methods

### Cyclostratigraphy and astronomically tuned age model

**Magnetic susceptibility measurements**: A total of 480 samples at 10 cm intervals spanning both the POE and the PETM weighing 4 to 8 grams were measured for bulk mass-normalized magnetic susceptibility (MS or $\chi$) using KLY-4S Kappabridge after being crushed in a copper rock hammer and placed in a $2\times2\times2$ $cm^3$ cubic plastic holder. The MS measurements were conducted at the Paleomagnetism and Environmental Magnetism Laboratory at the China University of Geoscience (Beijing). Measurements were made at room temperature with an applied field amplitude of 200 A/m and frequency of 976 Hz. Each measurement is corrected for the contribution of the plastic sample holder. Each sample was measured three times, with the average value corrected by mass to obtain $\chi$ in units of $m^3$ $kg^{-1}$. Relative standard deviations between the three runs were smaller than 0.5%.

**Time series analysis**: Time-series analysis was conducted using MS data with the open-source software Acycle V2.4[88] because MS measures the magnetic mineral concentration, and is considered as a proxy for detrital fluxes from land to the ocean[89]. The MS data series was first detrended by subtracting a 40-m "loess" trend (locally estimated scatterplot smoothing, a non-parametric method for a series of data smoothing with a default window size of 35%) to remove non-periodic or high-amplitude long-term trends following the procedures described in Li et al.[90]. The multi-taper method (MTM)[91] with $2\pi$ tapers was used to estimate the spectrum for the

390 detrended MS series and confidence levels (mean, 90%, 95%, and 99%) were
391 provided to test against robust first-order autoregressive model AR(1) red noise in
392 order to reveal the MS series' dominant wavelength. The evolutionary power spectra
393 were calculated with "Evolutionary Spectral Analysis" function in Acycle with a
394 sliding window of 10 m and a step of 0.1 m to identify any secular trend in dominant
395 frequencies, which may be attributed to variations in sedimentation rates. The time
396 scale optimization (TimeOpt; Meyers[92]) and correlation coefficient (COCO; Li et
397 al.[88]) methods were used to identify the optimal sedimentation rate using Acycle's
398 "COCO" and "TimeOpt" functions, which use 2,000 Monte Carlo statistical
399 simulations to test the null hypothesis of no orbital forcing. The evolutionary versions
400 of COCO and TimeOpt functions (i.e., eCOCO and eTimeOpt) were used to track
401 changes in sedimentation rates. In addition, the "Spectral Moments" function was
402 used to estimate variable sedimentation rates based on a periodogram with two
403 spectral moments: evolutionary mean frequency (μf) and evolutionary bandwidth (B)
404 (Figs. S4, S5). Subsequently, "Dynamic Filtering" function was used to apply
405 dynamic filtering and isolate interpreted precession cycles from the MS data series.
406 Since the power of long-term cycles (i.e., short eccentricity cycles) may have muted
407 the manifestation of precession cycles in the evolutive harmonic analysis (EHA), we
408 remove the > 4 m cycles that may be associated with eccentricity cycles to reveal
409 precession-related cycles as the most prominent signal in the EHA spectrogram (Fig.
410 S6). The significant power of the interpreted precession cycles in the EHA

411 spectrogram allows us to effectively isolate this signal from EHA (Fig. S4). We then
412 use the precession cycles to construct an astrochronological timescale for the study
413 interval. Analyses of TimeOpt and COCO indicate alternation of optimal
414 sedimentation rates (i.e., 6.0 cm $kyr^{-1}$ and 8.3 cm $kyr^{-1}$) (Fig. S4). Spectral Moments,
415 eTimeOpt and eCOCO together suggest the estimated sedimentation rate ranges from
416 4.2 to 10.6 cm $kyr^{-1}$ with increased sedimentation rate during the PETM body (Figs.
417 S5-S6).
418
419 **Stable carbon isotopes of bulk organic matter and wt.% $CaCO_3$**
420 HCl-treated carbonate-free powders were measured for total organic carbon
421 (TOC) and total nitrogen (TN) concentrations on a Vario EL-III elemental analyzer,
422 and the $\delta^{13}C_{org}$ analyses were made using a thermo DELTA plus XL mass
423 spectrometer at State Key Laboratory of Organic Geochemistry, Guangzhou Institute
424 of Geochemistry, Chinese Academy of Sciences. Three reference materials were used
425 to monitor the measurement of carbon isotopic ratio of bulk organic carbon, which
426 included black carbon (-22.43‰), Urea#1 (-34.13‰), and Urea#2 (-8.02‰).
427 Precision based on repeated measurement of these three standards were 0.12‰,
428 0.08‰, and 0.09‰, respectively. $\delta^{13}C_{org}$ values were reported in VPDB and analytical
429 precision was better than ±0.1‰ based on replicate analyses of the standards
430 processed with each batch of samples. Weight percent (wt.%) $CaCO_3$ was measured
431 using a modified acid soluble weight-loss method[93].

**Carbonate clumped isotope geochemistry**

The carbonate clumped isotope thermometer is based on the thermodynamic stability of C–O bonds at varying temperature, in which "clumping" of the rare, heavy isotopes of carbon and oxygen ($^{13}C$ and $^{18}O$) occurs more frequently at lower temperatures[94]. The excess occurrence of the $^{13}C^{18}O^{16}O$ isotopologue of $CO_2$ relative to a stochastic distribution of the heavy isotopes among all $CO_2$ molecules is referred to as the mass 47 anomaly and notated as $\Delta_{47}$, in which $\Delta_{47} = \left(\frac{^{47}R}{^{47}R^*}\right) \times 1000$ where $^{47}R = [^{13}C^{16}O^{18}O + ^{12}C^{17}O^{18}O + ^{13}C^{17}O_2]/[^{12}C^{16}O_2]$ and * denotes a stochastic distribution of isotopes. Clumped isotope thermometry presents a significant innovation over oxygen isotope-based thermometry because the temperature estimate is independent of the bulk isotopic composition, and thus requires no assumptions about $\delta^{18}O_{carb}$ or $\delta^{18}O_{water}$. This mineral formation temperature can be used to calculate $\delta^{18}O$ of ancient waters when paired with $\delta^{18}O_{carb}$ values of the same sample, which is measured concurrently with $\Delta_{47}$.

Carbonate clumped isotope measurements of one Eocene fossil oyster (*Crassostrea* sp.) and one modern oyster specimen (*Crassostrea hongkongensis*) collected from northern South China Sea (21°42'7.89" N, 111°55'44.61" E) in 2022 were made at the Pennsylvania State University in April 2022 (see SI). Approximately 8 mg of pure carbonate powder was digested in a 105% phosphoric acid common acid bath at 90 °C to yield $CO_2$. Evolved $CO_2$ was passed through a

Protium Isotope Batch Extraction (IBEX) carbonate preparation line to purify the sample gas. The gas is passed through a cryogenic trap to separate $CO_2$ from water, a silver wool-packed borosilicate column to trap sulfides, and a gas chromatography column packed with Poropak to separate $CO_2$ from other compounds with a He carrier gas. The purified $CO_2$ gas is once more frozen into a cryogenic trap before being frozen into a microvolume, and passed through a polished nickel capillary to the MAT 253 Plus bellows. Purified $CO_2$ sample gas was analyzed on a Thermo MAT253 Plus dual inlet IRMS relative to an Oztech working gas.

$\Delta_{47}$ values versus the working gas were projected to the Intercarb-Carbon Dioxide Equilibrium Scale[95] (I-CDES) using a carbonate standard-based empirical transfer function. ETH 1, 2, 3, and 4 were measured to build the reference frame and for interlaboratory comparison, and IAEA-C2 and Carrara Marble were treated as unknowns. Individual replicates were averaged to create final sample $\Delta_{47}$ values and reported with a 95% confidence interval. Temperatures were calculated using the T-$\Delta_{47}$ calibration of Anderson et al.[96]. The average measured $\Delta_{47}$ value for the oyster fossil is 0.573 ± 0.011 (2σ), while the $\Delta_{47}$ value for the modern oyster specimen is 0.604 ± 0.028 (2σ). The calculated sea surface temperature in the eastern Tethys based on early Eocene oyster fossil is 32.5 ± 3.9 °C (2σ). The calculated modern sea surface temperature based on modern oyster specimen is 21.6 ± 8.7 °C (2σ), falling in the range of the observed average annual sea surface temperature (24.1 ± 5.6 °C) in northern South China Sea in 2022.

474

475 **Biomarker and stable carbon isotopes of long-chain *n*-alkanes**

476 Around 11 grams of dried and powdered sample were extracted for their
477 biomarker content using a microwave system (Milestone Ethos EX) and using 20 ml
478 of a dichloromethane and methanol mixture (9:1). The total lipid extract was
479 separated using silica flash chromatography and elution with hexane:DCM (9:1) for
480 the apolar and DCM:MeOH (2:1) for the polar fraction. The apolar fractions were
481 characterized on a Thermo Scientific ISQ single quadrupole mass spectrometer (MS)
482 coupled to a gas chromatograph (GC). Compounds were separated using a fused silica
483 column (50 m × 0.32 mm) with a ZB1 stationary phase and helium as the carrier gas.
484 The GC was programmed for: injection at 70 °C (1 min hold), ramp to 130 °C at
485 20 °C/min, followed by a ramp to 300 °C at 4 °C/min (20 min hold). The MS
486 continuously scanned between *m/z* 650-50. The apolar fractions were subsequently
487 analyzed using an Isoprime 100 combustion isotope ratio mass spectrometer, coupled
488 to an Agilent GC, to determine the $\delta^{13}C$ of the long-chain *n*-alkanes. We used the
489 same type of column and temperature program as used for the GC-MS analyses.
490 Samples were measured in duplicate on the GC-C-IRMS, and the average is reported
491 here. An in-house $CO_2$ reference gas was used to calculate compound specific $\delta^{13}C$
492 values relative to Vienna Pee Dee Belemnite (VPDB). $\delta^{13}C$ values of the $C_{29}$ *n*-alkane
493 are not reported here due to possible co-elution with other lipids. All biomarker and

494 stable carbon isotopes of long-chain *n*-alkane analyses were performed at the
495 University of Bristol.
496
497 **Methods for GDGTs**
498 Polar fractions were filtered through a 0.45 μm filter at the university of
499 Bristol. The filtered polar fractions were redissolved in hexane:iso-propanol (99:1)
500 and analyzed using a high-pressure liquid chromatography atmospheric pressure
501 chemical ionization mass spectrometer for their GDGT distribution. We used two
502 ultra-high performance liquid chromatography silica columns to separate compounds,
503 following Hopmans et al. (2016)[97], and analyses were performed in selective ion
504 monitoring (SIM) mode.
505 The thermal maturity of the organic matter in this section was estimated using
506 the hopane isomerisation index: $C_{29}$ ββ/(αβ+βα+ ββ)[98]. The results indicate that the
507 thermal maturity changes across the section, but the $C_{29}$ ββ/(αβ+βα+ββ) ratio is
508 consistently below 0.4 (Fig. 3). This is indicative for an elevated thermal maturity, but
509 well below the oil window. Although this level of thermal maturity will not affect
510 apolar compounds like hopanoids or *n*-alkanes, it is likely to impact more labile
511 biomarkers such as glycerol dialkyl glycerol tetraethers (GDGTs)[99]. We determined
512 the GDGT distribution in all samples. As expected with this level of thermal maturity,
513 GDGT concentrations were low and, in most samples, branched (br)GDGTs were
514 absent, as were isoprenoidal (iso)GDGTs containing cyclopentane rings. However, a

few samples did have isoprenoidal (iso)GDGTs with cyclopentane rings. This includes the sample at depth 29.8 m that hosts the well-preserved oyster shell fossil. This sample has a $TEX_{86}$ value of 0.76, which results in an SST of 30.6 ± 4.5 °C using the $TEX_{86}^{H}$ calibration[100]. Although we treat this estimate cautious as thermal maturity might have impacted the GDGTs distribution, this $TEX_{86}$-based SST is consistent with the clumped isotope data from well-preserved oyster shell fossils from the same sample, adding confidence that we are able to constrain the SSTs at this site during the recovery phase of the PETM.

**Earth system modeling**

The carbon-centric Grid Enabled Integrated Earth system model (cGENIE) is an intermediate complexity climate model that couples a 3D ocean (36×36 grid, 16 levels) with a 2D atmosphere that has the capability to track biogeochemical cycling of elements, stable carbon isotopes, marine sediments, and continental weathering[12, 101]. Bathymetry, paleogeography, planetary albedo, and wind fields are configured for the late Paleocene-early Eocene with the same initial and boundary conditions as Gutjahr et al.[12]. For example, the $\delta^{13}C$ value of late Paleocene-early Eocene atmospheric $CO_2$ ($\delta^{13}C_{CO2}$) is set as ~ –5‰, and the atmospheric $pCO_2$ is set as ~830 ppmv. The moderately high $pCO_2$ allows for a small buildup of sea ice (0.5%) in the northern polar regions. We then run a number of 'double inversion' experiments in which $\delta^{13}C$ of surface ocean dissolved inorganic carbon ($\delta^{13}C_{DIC}$) and surface ocean

536 pH[19] are used as the two data assimilation constraints for the POE. The $\delta^{13}C_{DIC}$
537 forcing is based on the high-temporal-resolution $\delta^{13}C_{carb}$ data from the shallow Tethys
538 Kuzigongsu section using astronomically tuned age models. For our inversion
539 experiments, the model was first spun up for 20 kyr to establish the basic ocean
540 circulation and climatic state under published late Paleocene-early Eocene boundary
541 conditions, including paleogeography and paleobathymetry[102, 103]. This is followed by
542 an open-system spin-up of 200 kyr to allow the long-term $\delta^{13}C$ cycle to reach balance.
543 A range of inversion experiments were carried out (Table S3; Figs. S8-10). Although
544 uncertainty exists for pre-PETM $\delta^{11}B$, the surface ocean pH at the end of the open-
545 system spinup is 7.75, same as those used in Gutjahr et al. (2017)[12], which is adapted
546 as the initial surface ocean pH forcing in the "double inversion" experiment.
547 First, the "double-inversion" modeling takes the observed pH data, which
548 constrains the flux and magnitude of $CO_2$ emissions, and the observed $\delta^{13}C$ values of
549 the dissolved inorganic carbon of the surface ocean, which simultaneously determines
550 the source of the emitted carbon by computing the $\delta^{13}C$ values of the carbon source.
551 At each model time step, a pulse of $CO_2$ is emitted to the atmosphere at a given rate if
552 the $\delta^{13}C$ value is lower than the previous time step, and the modeled surface DIC $\delta^{13}C$
553 values and the observed $\delta^{13}C$ values at the Kuzigongsu section are compared. If the
554 current modeled surface DIC $\delta^{13}C$ value is higher than the data value, the $\delta^{13}C$ value
555 of the emitted $CO_2$ is assigned a value of –100‰. In contrast, if the current modeled
556 surface DIC $\delta^{13}C$ value is lower than the data value, the $\delta^{13}C$ value of the emitted $CO_2$

557 is assigned a value of 0‰. $\delta^{13}C$ values of the emitted $CO_2$ between –100‰ and 0‰
558 can be achieved by binning the emission fluxes in time and averaging flux-weighted
559 $\delta^{13}C$ values. Justification for the choice of these end-member $\delta^{13}C$ values of the
560 emitted $CO_2$ is provided in Gutjahr et al.[12]. During the experiments, cGENIE
561 continually adjusts the rate and $\delta^{13}C$ value of emitted $CO_2$ into the atmosphere in
562 order to simultaneously reproduce the two proxy records as a function of time. In
563 these experiments, we assume that the POE onset occurred as a linear decline in both
564 $\delta^{13}C$ and pH simultaneously (Fig. 4a, b). We use the same "double-inversion"
565 methodology in both the main experiments and the sensitivity experiments, both
566 starting from the same open-system spin-up state (Table S3).

567 **Sensitivity experiments and analyses**

568 We carried out sensitivity experiments to explore the importance of the
569 duration of the POE onset (~7,000, ~1,600, ~850, and ~500 years based on age model
570 option 1, age model option 2, Bowen et al. (2016), and Babila et al. (2022),
571 respectively) using a global compilation of marine carbonate $\delta^{13}C_{carb}$ records (Table
572 S3; Fig. S8). We also tested the effect of larger pH decrease (i.e., –0.24 and –0.32 pH
573 unit) in combination with each of the four assumed age model (Table S3).
574 Additionally, we test the role of bioturbation on the carbon isotope excursion
575 magnitude of core-top carbonates (Fig. S10).

576

**Data availability**. Bulk carbonate, organic matter and compound specific stable isotope data can be found in Supplementary Information. All modelling-related data are included as part of the cGENIE model code distribution (see above).

**Code availability**. The code for the version of the 'muffin' release of the cGENIE Earth system model used in this paper, is tagged as vxxx, and is assigned a DOI: xxx. Configuration files for the specific experiments presented in the paper can be found in the directory: genie-userconfigs/PUBS/submitted/Jiang_et_al.NC.2022. Details of the experiments, plus the command line needed to run each one, are given in the readme.txt file in that directory. All other configuration files and boundary conditions are provided as part of the code release. A manual detailing code installation, basic model configuration, tutorials covering various aspects of model configuration, experimental design, and output, plus the processing of results, is assigned a DOI: xxx.

## References


1. McInerney FA, Wing SL. The Paleocene-Eocene Thermal Maximum: A perturbation of carbon cycle, climate, and biosphere with implications for the future. *Annual Review of Earth and Planetary Sciences* **39**, 489-516 (2011).

2. Zhu J, Poulsen CJ, Tierney JE. Simulation of Eocene extreme warmth and high climate sensitivity through cloud feedbacks. *Science Advances* **5**, eaax1874 (2019).

3. Tierney JE*, et al.* Spatial patterns of climate change across the Paleocene-Eocene Thermal Maximum. *Proceedings of the National Academy of Sciences* **119**, e2205326119 (2022).

4. Zachos JC*, et al.* Rapid Acidification of the Ocean During the Paleocene-Eocene Thermal Maximum. *Science* **308**, 1611-1615 (2005).

5. Yao W, Paytan A, Wortmann UG. Large-scale ocean deoxygenation during the Paleocene-Eocene Thermal Maximum. *Science* **361**, 804-806 (2018).

6. Mariani E*, et al.* Large Igneous Province Control on Ocean Anoxia and Eutrophication in the North Sea at the Paleocene–Eocene Thermal Maximum. *Paleoceanography and Paleoclimatology* **39**, e2023PA004756 (2024).

7. Yao W, Kong T, Wang XT, Zhai R, Zhang R, Liu Y. Expanded subsurface ocean anoxia in the Atlantic during the Paleocene-Eocene Thermal Maximum. *Nature Communications* **15**, 9053 (2024).

8. Wu Q, Cui Y, Wang Y, Jiang S, Dong Y, Shen J. Biogeochemical responses to global warming during the Paleocene–Eocene Thermal Maximum in the eastern Tethys. *Palaeogeography, Palaeoclimatology, Palaeoecology*, 111969 (2023).

9. Rush WD, Kiehl JT, Shields CA, Zachos JC. Increased frequency of extreme precipitation events in the North Atlantic during the PETM: Observations and theory. *Palaeogeography, Palaeoclimatology, Palaeoecology*, 110289 (2021).

10. Kiehl JT, Zarzycki CM, Shields CA, Rothstein MV. Simulated changes to tropical cyclones across the Paleocene-Eocene Thermal Maximum (PETM) boundary. *Palaeogeography, Palaeoclimatology, Palaeoecology* **572**, 110421 (2021).

11. Cui Y*, et al.* Slow release of fossil carbon during the Palaeocene-Eocene Thermal Maximum. *Nature Geoscience* **4**, 481-485 (2011).

12. Gutjahr M*, et al.* Very large release of mostly volcanic carbon during the Palaeocene–Eocene Thermal Maximum. *Nature* **548**, 573-577 (2017).

13. Jones SM, Hoggett M, Greene SE, Jones TD. Large Igneous Province thermogenic greenhouse gas flux could have initiated Paleocene-Eocene Thermal Maximum climate change. *Nature Communications* **10**, 1-16 (2019).

14. Gernon TM*, et al.* Transient mobilization of subcrustal carbon coincident with Palaeocene–Eocene Thermal Maximum. *Nature Geoscience*, (2022).

15. Jones MT*, et al.* Mercury anomalies across the Palaeocene–Eocene thermal maximum. *Climate of the Past* **15**, 217-236 (2019).

16. Bowen GJ, Zachos JC. Rapid carbon sequestration at the termination of the Palaeocene-Eocene Thermal Maximum. *Nature Geoscience* **3**, 866-869 (2010).

17. Penman DE. Silicate weathering and North Atlantic silica burial during the Paleocene-Eocene Thermal Maximum. *Geology* **44**, 731-734 (2016).

18. Bowen GJ*, et al.* Two massive, rapid releases of carbon during the onset of the Palaeocene-Eocene thermal maximum. *Nature Geoscience* **8**, 44-47 (2015).

19. Babila TL*, et al.* Surface ocean warming and acidification driven by rapid carbon release precedes Paleocene-Eocene Thermal Maximum. *Science Advances* **8**, eabg1025 (2022).

20. Crouch EM, Brinkhuis H, Visscher H, Adatte T, Bolle M-P. Late Paleocene-early Eocene dinoflagellate cyst records from the Tethys; further observations on the global distribution of Apectodinium. In: *Special Paper - Geological Society of America, vol.369* (eds Wing SL, Gingerich PD, Schmitz B, Thomas E) (2003).

21. Sluijs A*, et al.* Environmental precursors to rapid light carbon injection at the Palaeocene/Eocene boundary. *Nature* **450**, 1218-1221 (2007).

22. Tremblin M*, et al.* Mercury enrichments of the Pyrenean foreland basins sediments support enhanced volcanism during the Paleocene-Eocene thermal maximum (PETM). *Global and Planetary Change*, 103794 (2022).

23. Stokke EW, *et al.* Rapid and sustained environmental responses to global warming: the Paleocene–Eocene Thermal Maximum in the eastern North Sea. *Clim Past* **17**, 1989-2013 (2021).

24. Bowen GJ, *et al.* Two massive, rapid releases of carbon during the onset of the Palaeocene–Eocene thermal maximum. *Nature Geoscience* **8**, 44-47 (2015).

25. Bralower TJ, *et al.* Impact of dissolution on the sedimentary record of the Paleocene-Eocene thermal maximum. *Earth and Planetary Science Letters* **401**, 70-82 (2014).

26. Zeebe RE, Westerhold T, Littler K, Zachos JC. Orbital forcing of the Paleocene and Eocene carbon cycle. *Paleoceanography*, (2017).

27. Lourens LJ, *et al.* Astronomical pacing of late Palaeocene to early Eocene global warming events. *Nature* **435**, 1083-1087 (2005).

28. Zeebe RE, Ridgwell A, Zachos JC. Anthropogenic carbon release rate unprecedented during the past 66 million years. *Nature Geoscience* **9**, 325-329 (2016).

29. Wieczorek R, Fantle MS, Kump LR, Ravizza G. Geochemical evidence for volcanic activity prior to and enhanced terrestrial weathering during the Paleocene Eocene Thermal Maximum. *Geochimica et Cosmochimica Acta* **119**, 391-410 (2013).

30. Jiang J, *et al.* Eustatic change across the Paleocene-Eocene Thermal Maximum in the epicontinental Tarim seaway. *Global and Planetary Change* **229**, 104241 (2023).

31. Kaya MY, *et al.* The Eurasian epicontinental sea was an important carbon sink during the Palaeocene-Eocene thermal maximum. *Communications Earth & Environment* **3**, 124 (2022).

32. Wang Y, *et al.* Response of calcareous nannoplankton to the Paleocene–Eocene Thermal Maximum in the Paratethys Seaway (Tarim Basin, West China). *Global and Planetary Change*, 103918 (2022).

33. Diefendorf AF, Mueller KE, Wing SL, Koch PL, Freeman KH. Global patterns in leaf $^{13}C$ discrimination and implications for studies of past and

future climate. *Proceedings of the National Academy of Sciences* **107**, 5738-5743 (2010).

34. Cui Y, Schubert BA. Towards determination of the source and magnitude of atmospheric pCO2 change across the early Paleogene hyperthermals. *Global and Planetary Change* **170**, 120-125 (2018).

35. Knauth LP, Kennedy MJ. The late Precambrian greening of the Earth. *Nature*, (2009).

36. Derry LA. A burial diagenesis origin for the Ediacaran Shuram-Wonoka carbon isotope anomaly. *Earth and Planetary Science Letters* **294**, 152-162 (2010).

37. Röhl U, Westerhold T, Bralower TJ, Zachos JC. On the duration of the Paleocene-Eocene thermal maximum (PETM). *Geochemistry, Geophysics, Geosystems* **8**, Q12002 (2007).

38. Zeebe RE, Lourens LJ. Solar System chaos and the Paleocene–Eocene boundary age constrained by geology and astronomy. *Science* **365**, 926-929 (2019).

39. Bralower TJ*, et al.* Evidence for Shelf Acidification during the Onset of the Paleocene- Eocene Thermal Maximum. *Paleoceanography and Paleoclimatology*, (2018).

40. Bralower TJ*, et al.* Evidence for shelf acidification during the onset of the Paleocene- Eocene Thermal Maximum. *Paleoceanography and Paleoclimatology* **33**, 1408-1426 (2018).

41. Naafs BDA, Castro JM, De Gea GA, Quijano ML, Schmidt DN, Pancost RD. Gradual and sustained carbon dioxide release during Aptian Oceanic Anoxic Event 1a. *Nature Geoscience* **9**, 135 (2016).

42. De Palma M*, et al.* Stable isotopes of black carbon and their implications to paleoclimate in the eastern Tethys during the PETM. *Palaeogeography, Palaeoclimatology, Palaeoecology*, 112794 (2025).

43. Wu Q, Cui Y, Wang Y, Jiang S, Dong Y, Shen J. Biogeochemical responses to global warming during the Paleocene–Eocene Thermal Maximum in the eastern Tethys. *Palaeogeography, Palaeoclimatology, Palaeoecology* **636**, 111969 (2024).

44. Sinninghe Damsté JS, Schouten S, Hopmans EC, van Duin ACT, Geenevasen JAJ. Crenarchaeol. *Journal of Lipid Research* **43**, 1641-1651 (2002).

45. Qin W*, et al.* Confounding effects of oxygen and temperature on the TEX86 signature of marine Thaumarchaeota. *Proceedings of the National Academy of Sciences* **112**, 10979-10984 (2015).

46. Summons R, Jahnke L, Hope J, Logan G. 2-Methylhopanoids as biomarkers for cyanobacterial oxygenic photosynthesis. **400**, 554-557 (1999).

47. Newman DK, Neubauer C, Ricci JN, Wu C-H, Pearson A. Cellular and molecular biological approaches to interpreting ancient biomarkers. *Annual Review of Earth and Planetary Sciences* **44**, 493-522 (2016).

48. Ricci JN*, et al.* Diverse capacity for 2-methylhopanoid production correlates with a specific ecological niche. *The ISME Journal* **8**, 675-684 (2014).

49. Schaefer B, Schwark L, Böttcher ME, Smith V, Coolen MJL, Grice K. Paleoenvironmental evolution during the Early Eocene Climate Optimum in the Chicxulub impact crater. *Earth and Planetary Science Letters* **589**, 117589 (2022).

50. Garby TJ*, et al.* Lack of methylated hopanoids renders the cyanobacterium Nostoc punctiforme sensitive to osmotic and pH stress. *Applied and Environmental Microbiology* **83**, e00777-00717 (2017).

51. Xie S, Pancost RD, Yin H, Wang H, Evershed RP. Two episodes of microbial change coupled with Permo/Triassic faunal mass extinction. *Nature* **434**, 494-497 (2005).

52. Kasprak AH*, et al.* Episodic photic zone euxinia in the northeastern Panthalassic Ocean during the end-Triassic extinction. *Geology*, G36371. 36371 (2015).

53. Naafs BDA, Bianchini G, Monteiro FM, Sánchez- Baracaldo P. The occurrence of 2- methylhopanoids in modern bacteria and the geological record. *Geobiology* **20**, 41-59 (2022).

54. Kuypers MM, van Breugel Y, Schouten S, Erba E, Damsté JSS. $N_2$-fixing cyanobacteria supplied nutrient N for Cretaceous oceanic anoxic events. *Geology* **32**, 853-856 (2004).

55. Cullers RL. Implications of elemental concentrations for provenance, redox conditions, and metamorphic studies of shales and limestones near Pueblo, CO, USA. *Chemical Geology* **191**, 305-327 (2002).

56. Wedepohl KH. Manganese: abundance in common sediments and sedimentary rocks. *Handbook of Geochemistry: Berlin, Springer* **2**, 1-17 (1978).

57. Tribovillard N, Algeo T, Lyons T, Riboulleau A. Trace metals as paleoredox and paleoproductivity proxies: An update. *Chemical Geology* **232**, 12-32 (2006).

58. Zhou X, Thomas E, Rickaby R, Winguth A, Lu Z. I/Ca evidence for upper ocean deoxygenation during the PETM. *Paleoceanography* **29**, 964-975 (2014).

59. Schoon PL, Heilmann-Clausen C, Schultz BP, Damsté JSS, Schouten S. Warming and environmental changes in the eastern North Sea Basin during the Palaeocene–Eocene Thermal Maximum as revealed by biomarker lipids. *Organic Geochemistry* **78**, 79-88 (2015).

60. Stein R, Boucsein B, Meyer H. Anoxia and high primary production in the Paleogene central Arctic Ocean: First detailed records from Lomonosov Ridge. *Geophysical Research Letters* **33**, (2006).

61. Stassen P, Thomas E, Speijer RP. Paleocene–Eocene Thermal Maximum environmental change in the New Jersey Coastal Plain: benthic foraminiferal biotic events. *Marine Micropaleontology* **115**, 1-23 (2015).

62. Sluijs A*, et al.* Warming, euxinia and sea level rise during the Paleocene–Eocene Thermal Maximum on the Gulf Coastal Plain: implications for ocean oxygenation and nutrient cycling. *Climate of the Past* **10**, 1421-1439 (2014).

63. Behrooz L*, et al.* North- East Peri- Tethyan Water Column Deoxygenation and Euxinia at the Paleocene Eocene Thermal Maximum. *Paleoceanography and Paleoclimatology* **39**, e2023PA004828 (2024).

64. Dong Y*, et al.* Paleoenvironment reconstruction of the eastern Tethys during the pre-onset excursion preceding the PETM. *Palaeogeography, Palaeoclimatology, Palaeoecology*, 112234 (2024).

65. Kender S*, et al.* Paleocene/Eocene carbon feedbacks triggered by volcanic activity. *Nature Communications* **12**, 1-10 (2021).

66. Fendley IM, Mittal T, Sprain CJ, Marvin-DiPasquale M, Tobin TS, Renne PR. Constraints on the volume and rate of Deccan Traps flood basalt eruptions using a combination of high-resolution terrestrial mercury records and geochemical box models. *Earth and Planetary Science Letters* **524**, 115721 (2019).

67. Denis EH, Pedentchouk N, Schouten S, Pagani M, Freeman KH. Fire and ecosystem change in the Arctic across the Paleocene–Eocene Thermal Maximum. *Earth and Planetary Science Letters*, (2017).

68. Moore EA, Kurtz AC. Black carbon in Paleocene–Eocene boundary sediments: A test of biomass combustion as the PETM trigger. *Palaeogeography, Palaeoclimatology, Palaeoecology* **267**, 147-152 (2008).

69. Collinson ME, Steart D, Scott A, Glasspool I, Hooker J. Episodic fire, runoff and deposition at the Palaeocene–Eocene boundary. *Journal of the Geological Society* **164**, 87-97 (2007).

70. Sanei H, Grasby SE, Beauchamp B. Latest Permian mercury anomalies. *Geology* **40**, 63-66 (2012).

71. Grasby SE, Them TR, Chen Z, Yin R, Ardakani OH. Mercury as a proxy for volcanic emissions in the geologic record. *Earth-Science Reviews* **196**, 102880 (2019).

72. Jones MT*, et al.* Tracing North Atlantic volcanism and seaway connectivity across the Paleocene–Eocene Thermal Maximum (PETM). *Climate of the Past* **19**, 1623-1652 (2023).

73. Storey M, Duncan RA, Swisher III CC. Paleocene-Eocene thermal maximum and the opening of the northeast Atlantic. *Science* **316**, 587-589 (2007).

74. Storey M, Duncan RA, Tegner C. Timing and duration of volcanism in the North Atlantic Igneous Province: Implications for geodynamics and links to the Iceland hotspot. *Chemical Geology* **241**, 264-281 (2007).

75. Wilkinson CM, Ganerød M, Hendriks BW, Eide EA. Compilation and appraisal of geochronological data from the North Atlantic Igneous Province

(NAIP). *Geological Society, London, Special Publications* **447**, 69-103 (2017).

76. Larsen RB, Tegner C. Pressure conditions for the solidification of the Skaergaard intrusion: Eruption of East Greenland flood basalts in less than 300,000years. *Lithos* **92**, 181-197 (2006).

77. Dickson AJ, Cohen AS, Coe AL, Davies M, Shcherbinina EA, Gavrilov YO. Evidence for weathering and volcanism during the PETM from Arctic Ocean and Peri-Tethys osmium isotope records. *Palaeogeography, Palaeoclimatology, Palaeoecology* **438**, 300-307 (2015).

78. Liu Z*, et al.* Assessing the Contributions of Comet Impact and Volcanism Towards the Climate Perturbations of the Paleocene–Eocene Thermal Maximum. *Geophysical Research Letters*, (2019).

79. Berndt C*, et al.* Shallow-water hydrothermal venting linked to the Palaeocene–Eocene Thermal Maximum. *Nature Geoscience*, (2023).

80. Frieling J, Svensen HH, Planke S, Cramwinckel MJ, Selnes H, Sluijs A. Thermogenic methane release as a cause for the long duration of the PETM. *Proceedings of the National Academy of Sciences* **113**, 12059-12064 (2016).

81. Zeebe RE, Zachos JC, Dickens GR. Carbon dioxide forcing alone insufficient to explain Palaeocene–Eocene Thermal Maximum warming. *Nature Geoscience* **2**, 576-580 (2009).

82. Turner SK. Constraints on the onset duration of the Paleocene–Eocene Thermal Maximum. *Philosophical Transactions of the Royal Society A: Mathematical, Physical and Engineering Sciences* **376**, 20170082 (2018).

83. Schoell M. The hydrogen and carbon isotopic composition of methane from natural gases of various origins. *Geochimica et Cosmochimica Acta* **44**, 649-661 (1980).

84. Niemann H, Elvert M. Diagnostic lipid biomarker and stable carbon isotope signatures of microbial communities mediating the anaerobic oxidation of methane with sulphate. *Organic Geochemistry* **39**, 1668-1677 (2008).

85. Blumenberg M, Seifert R, Reitner J, Pape T, Michaelis W. Membrane lipid patterns typify distinct anaerobic methanotrophic consortia. *Proceedings of the National Academy of Sciences* **101**, 11111-11116 (2004).

86. Penman DE, Hönisch B, Zeebe RE, Thomas E, Zachos JC. Rapid and sustained surface ocean acidification during the Paleocene- Eocene Thermal Maximum. *Paleoceanography* **29**, 357-369 (2014).

87. Kirtland Turner S, Ridgwell A. Recovering the true size of an Eocene hyperthermal from the marine sedimentary record. *Paleoceanography* **28**, 700-712 (2013).

88. Li M, Hinnov L, Kump L. Acycle: Time-series analysis software for paleoclimate research and education. *Computers & Geosciences* **127**, 12-22 (2019).

89. Kodama KP, Hinnov LA. *Rock magnetic cyclostratigraphy*. John Wiley & Sons (2014).

90. Li M*, et al.* Astrochronology of the Paleocene-Eocene Thermal Maximum on the Atlantic Coastal Plain. *Nature Communications* **13**, 5618 (2022).

91. Thomson DJ. Spectrum estimation and harmonic analysis. *Proceedings of the IEEE* **70**, 1055-1096 (1982).

92. Meyers SR. The evaluation of eccentricity- related amplitude modulation and bundling in paleoclimate data: An inverse approach for astrochronologic testing and time scale optimization. *Paleoceanography* **30**, 1625-1640 (2015).

93. Molnia BF. A rapid and accurate method for the analysis of calcium carbonate in small samples. *Journal of Sedimentary Research* **44**, 589-590 (1974).

94. Eiler JM. "Clumped-isotope" geochemistry: The study of naturally-occurring, multiply-substituted isotopologues. *Earth and Planetary Science Letters* **262**, 309-327 (2007).

95. Bernasconi SM*, et al.* InterCarb: A community effort to improve interlaboratory standardization of the carbonate clumped isotope thermometer using carbonate standards. *Geochemistry, Geophysics, Geosystems* **22**, e2020GC009588 (2021).

96. Anderson N*, et al.* A unified clumped isotope thermometer calibration (0.5–1,100 C) using carbonate- based standardization. *Geophysical Research Letters* **48**, e2020GL092069 (2021).

97. Hopmans EC, Schouten S, Damsté JSS. The effect of improved chromatography on GDGT-based palaeoproxies. *Organic Geochemistry* **93**, 1-6 (2016).

98. Mackenzie AS, Patience RL, Maxwell JR, Vandenbroucke M, Durand B. Molecular parameters of maturation in the Toarcian shales, Paris Basin, France—I. Changes in the configurations of acyclic isoprenoid alkanes, steranes and triterpanes. *Geochimica et Cosmochimica Acta* **44**, 1709-1721 (1980).

99. Schouten S, Hopmans EC, Sinninghe Damsté JS. The effect of maturity and depositional redox conditions on archaeal tetraether lipid palaeothermometry. *Organic Geochemistry* **35**, 567-571 (2004).

100. Kim J-H*, et al.* New indices and calibrations derived from the distribution of crenarchaeal isoprenoid tetraether lipids: Implications for past sea surface temperature reconstructions. *Geochimica et Cosmochimica Acta* **74**, 4639-4654 (2010).

101. Ridgwell A, Schmidt DN. Past constraints on the vulnerability of marine calcifiers to massive carbon dioxide release. *Nature Geoscience* **3**, 196-200 (2010).

102. Bice KL, Barron EJ, Peterson WH. Reconstruction of realistic early Eocene paleobathymetry and ocean GCM sensitivity to specified basin configuration. *Oxford Monographs on Geology and Geophysics* **39**, 227-250 (1998).

103. Kirtland Turner S, Ridgwell A. Development of a novel empirical framework for interpreting geological carbon isotope excursions, with implications for the rate of carbon injection across the PETM. *Earth and Planetary Science Letters* **435**, 1-13 (2016).

104. Yong T. Lithofacies and Paleogeography of The Late Cretaceous-Early Tertiary of the Tarim Platform (in Chinese with English abstract). *Experimental Petroleum Geology* **6**, 9-17 (1984).

105. Lippert PC, van Hinsbergen DJJ, Dupont-Nivet G. Early Cretaceous to present latitude of the central proto-Tibetan Plateau: A paleomagnetic synthesis with implications for Cenozoic tectonics, paleogeography, and climate of Asia. In: *Toward an Improved Understanding of Uplift Mechanisms and the Elevation History of the Tibetan Plateau* (eds Nie J, Horton BK, Hoke GD). Geological Society of America (2014).

1009
1010
1011

**Acknowledgments**

We thank Zhilin Yang for field assistance, and Hong Su for providing technical support and Isabel M. Fendley for discussions on mercury data interpretation. S.J. and Y.W. are supported by the National Key R&D Program of China (2022YFF0800800) and NSFC grants 41888101 & 41976045 & 42206047, Y.C. is supported by NSF Award 2002370. J.W. thanks the Agouron Institute for support. B.D.A.N. thanks the NERC (contract no. NE/V003917/1) and funding from the European Research Council under the European Union's Seventh Framework Programme (FP/2007-2013) and European Research Council Grant Agreement number 340923 for partial funding of the National Environmental Isotope Facility and GC-MS, GC-C-IRMS, and HPLC-MS capabilities at the OGU in Bristol. B.D.A.N. was funded through a Royal Society Tata University Research Fellowship. A.R. acknowledges support from NSF (EAR 2121165 and MG&G 2244897). This manuscript is a contribution to IGCP 739 project.

**Author contributions**

S.J. and Y.C. designed the study and interpreted the data. Y.C., M.D.P. and A.R. performed and analyzed cGENIE modeling experiments. B.D.A.N. and Y.H. led the biomarker data acquisition. Y.W., S.J. and Y.G. interpreted the calcareous nannofossil biostratigraphy and performed XRF analysis, H.W. and R.C. performed age model, J.J. and X.H. conducted sedimentology. M.I. performed clumped isotope analysis. S.J.

and Y.C. wrote the manuscript with inputs from T.B., A.R., J.Z., B.D.A.N., J.W., H.W., R.C., S.Y., and M.I.

## Competing interests

The authors declare that they have no competing interests.

## Figure captions

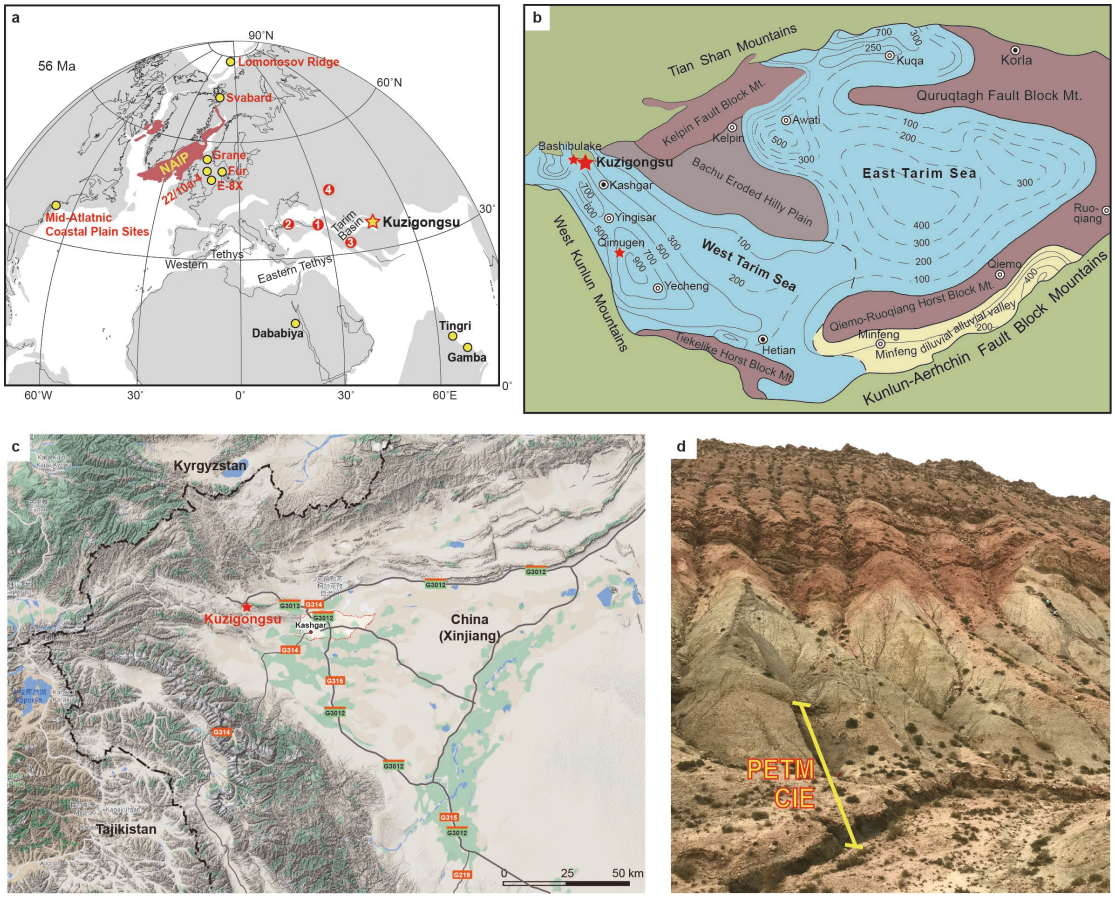


**Figure 1.** (**a, b**), Paleogeographic setting of the study area in the early Paleogene[104, 105], (**c**), present location of the study site Kuzigongsu Section and (**d**), a photo of the outcrop. Panel (**a**) also shows other shallow water PETM records in Aktumsuk (1), Kheu River and Guru-Fatima (2-3), West Siberian Well 10 (4), southern Tibet (Tingri and Gamba), Tarim Basin, Denmark (E-8X, 22/10a-4, Grane, and Fur), Svalbard, Arctic (Lomonosov Ridge), and Mid-Atlantic Coastal Plain Sites (Ancora, Wilson Lake, Clayton, and Millville located in the New Jersey, and South Dover Bridge or SDB and Cambridge-Dorchester Airport located in the Salisbury Embayment in Maryland)**.** References associated with these sites are listed in Table S3.

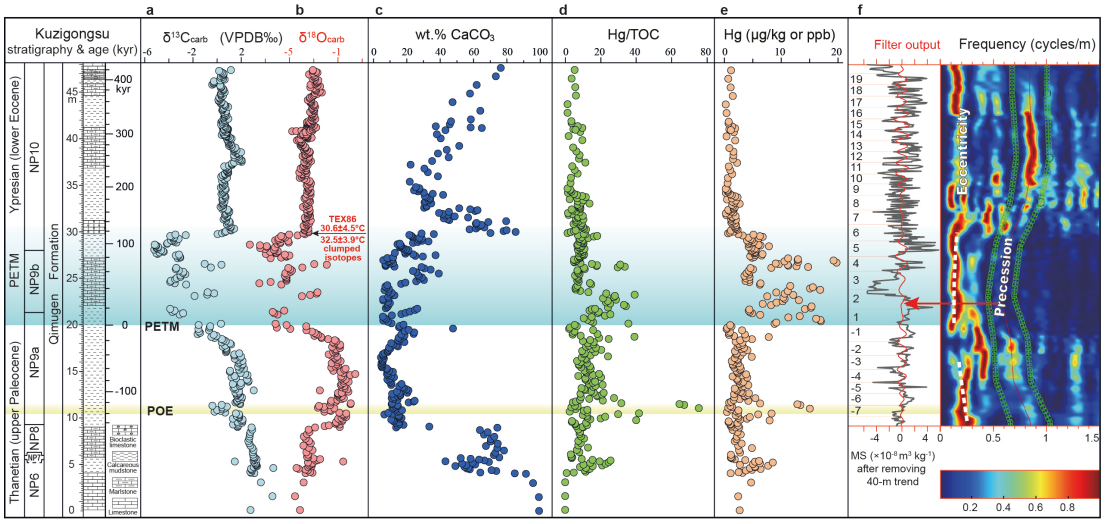


**Figure 2.** Characteristics of the PETM and POE records at the Kuzigongsu section, eastern Tethys. (**a**, **b**), $\delta^{13}C_{carb}$ and $\delta^{18}O_{carb}$ from Wang et al. (2022)[32]. Note the two novel sea surface temperature estimates based on oyster fossil $\Delta_{47}$ and $TEX_{86}^{H}$ at 29.8 m depth. (**c**), wt.% $CaCO_3$. (**d**), Hg/TOC ratio. (**e**), Hg concentration. (**f**), astronomically tuned age model based on magnetic susceptibility (MS) across the POE and PETM. The color bar represents spectral power and the green band represents the bandwidth of the precession cycles. Numbers in (**f**) indicate precession

cycles assignments.

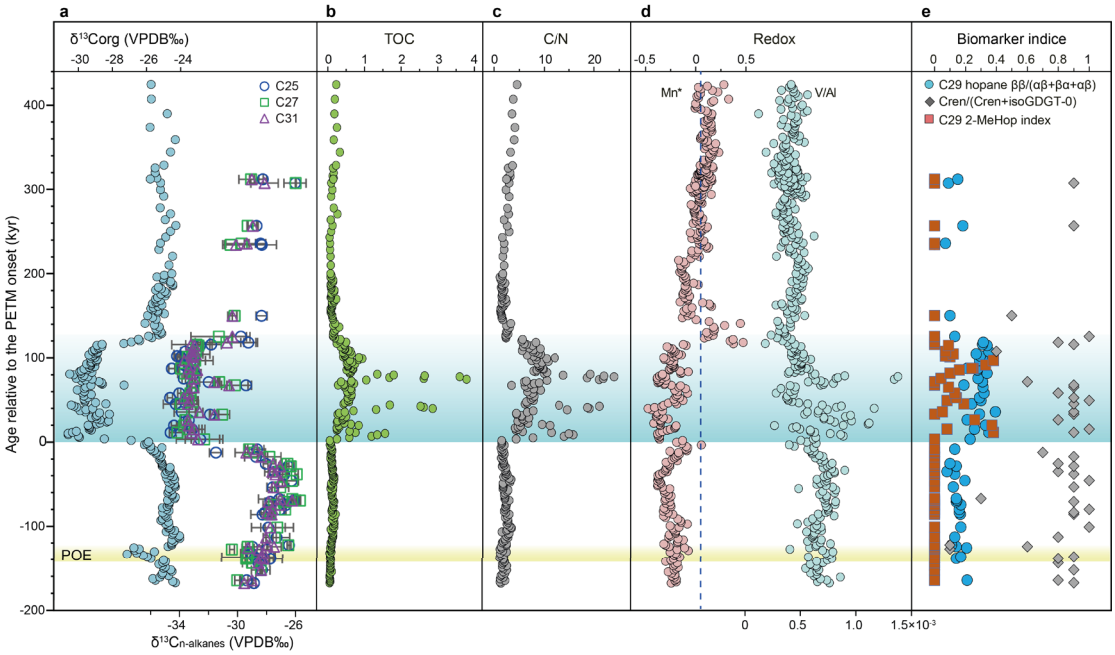


**Figure 3.** Proxy-based reconstruction of environmental changes across the PETM and POE at the Kuzigongsu section, eastern Tethys. Relative age from the onset of the PETM is based on an astronomically tuned age model described in SI. (**a**) $\delta^{13}C_{org}$ from bulk organic matter and $\delta^{13}C_{n\text{-alkanes}}$ from long-chain *n*-alkanes ($nC_{25}$ in blue circles, $nC_{27}$ in green squares, and $nC_{31}$ in purple triangles); (**b**) Total organic carbon content (TOC); (**c**) organic carbon to nitrogen ratio (C/N); (**d**) Mn* (pink circles)[64] and V/Al ratio (orange circles) as redox proxies; (**e**) Biomarker indices based on $C_{29}$ hopane ββ/(αβ+βα+αβ) (blue circles), Crenarchaeol/(Crenarchaeol+isoGDGT-0) or Cren/(Cren+isoGDGT-0) (dark blue diamond), and $C_{29}$ 2-Methylhopane index (2-MeHop) (red squares).

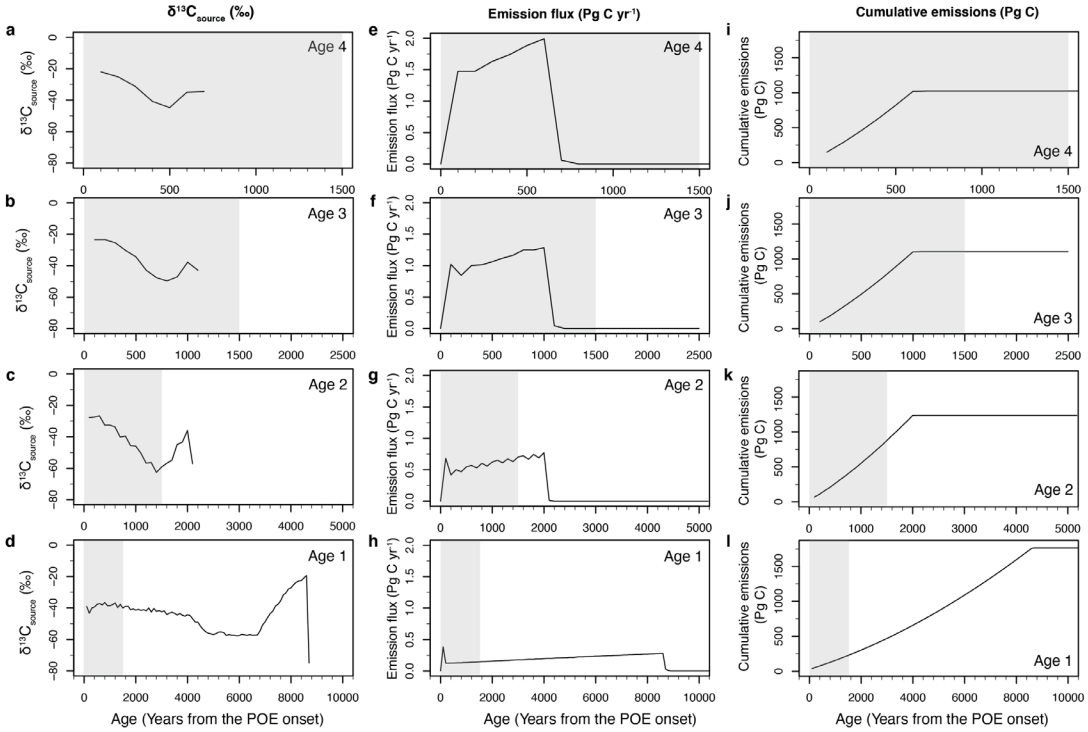


**Figure 4.** Data assimilation results from our cGENIE Earth system modeling based on the pH-$\delta^{13}C_{DIC}$ double inversion of four scenarios based on different assumptions of POE onset duration. (**a-d**), $\delta^{13}C_{source}$ values of the diagnosed carbon source for the four age models (see age model interpretation in the main text). (**e-h**), Model-diagnosed rates of $CO_2$ emission for the four age models. (**i-l**), Cumulative amount of $CO_2$ emitted for the four age models. The gray shaded area represents 1,500 years.